

Nitrogen split interstitial center (N-N)_N in GaN: High frequency EPR and ENDOR study

H. J. von Bardeleben and J. L. Cantin

Sorbonne Universités, UPMC Université Paris 06, UMR7588, Institut des Nanosciences de Paris, 4 place Jussieu, 75005 Paris, France

H. Vrielinck and F. Callens

Department of Solid State Sciences, Ghent University, Krijgslaan 281-S1, B-9000 Ghent, Belgium

L. Binet

Institut de Recherche de Chimie-Paris CNRS – Chimie ParisTech 11, rue Pierre et Marie Curie, 75005 Paris, France

E. Rauls and U. Gerstmann

Lehrstuhl für Theoretische Physik, Universität Paderborn, 33098 Paderborn, Germany

(Received 3 July 2014; revised manuscript received 4 August 2014; published 18 August 2014)

The nitrogen split interstitial defect introduced by high-energy particle irradiation in *n*-type GaN has been investigated by very high (up to 324 GHz) frequency electron paramagnetic resonance (EPR) and *Q*-band electron nuclear double resonance (ENDOR) spectroscopy. The increased resolution of the EPR spectra at 324 GHz has allowed us to determine the *g*-tensor anisotropy, which is not resolved at *X* or *Q* band. The good agreement of the principal values $g_{xx} = 1.9966$, $g_{yy} = 2.0016$, and $g_{zz} = 2.0036$ with the theoretically predicted *g* tensor confirm the (N-N)_N⁰ defect model. The hyperfine interactions of this defect have been studied by *Q*-band ENDOR. We observed well-resolved ENDOR lines with distant Ga atoms from which the quadrupole coupling constants and the electrical field gradients were determined and discussed with the help of theoretical values. The observation of ENDOR spectra of the central N and Ga atoms predicted in the 20–90-MHz range required the use of field-frequency ENDOR due to the large linewidth of the ENDOR lines. Our results confirm the importance of the nitrogen split interstitial in particle irradiated GaN similar to the case of diamond and silicon carbide in which the stable configuration at room temperature of the carbon interstitials is also the split interstitial configuration.

DOI: [10.1103/PhysRevB.90.085203](https://doi.org/10.1103/PhysRevB.90.085203)

PACS number(s): 71.55.Eq, 71.15.–m, 76.30.Mi, 78.70.Bj

I. INTRODUCTION

GaN is an important technological semiconductor material, which is now widely applied in micro- and optoelectronics devices. As for all semiconductors, a major issue is the stability/degradation of GaN based devices when exposed to high temperatures or particle irradiation. Under such conditions individual intrinsic point defects and clusters of defects are generated and will modify the electronic properties of GaN films and can even give rise to extended defect formation. The main defects generated by irradiation or high-temperature treatments are intrinsic defects such as vacancies, interstitials, or their complexes. Due to the large band gap of GaN most of the intrinsic defects introduce more than one charge transition level and may act as acceptors (V_{Ga}), donors (V_{N} , Ga_{int}) or are amphoteric such as N_{int} . Thus, their generation by irradiation or ion implantation will lead to electrical compensation and failure of GaN based devices. It is thus not surprising that defects, introduced by particle irradiation, or more generally, intrinsic defects, have been studied in GaN for more than two decades both experimentally and theoretically. The main experimental techniques used are magnetic resonance [1–8], positron annihilation spectroscopy [9–15], and electrical measurements [16–19]. Different theoretical studies of intrinsic defects in GaN have been published [20–24]. For a review see for example Refs. [4,20,24].

In spite of many efforts the experimental assessment of the intrinsic defects in GaN is still very limited. It might seem surprising that electron paramagnetic resonance (EPR), the main technique which allowed in the past a detailed description

of the microscopic structure of the intrinsic defects in other semiconductors such as Si, SiC, GaAs, or ZnO, has only rarely been applied with success in the case of GaN. Most magnetic resonance studies have been performed by optically detected magnetic resonance (ODMR). ODMR has the advantage of higher sensitivity but leads to increased linewidth as compared to EPR. Various paramagnetic defects have been evidenced in as-grown and irradiated samples but due to the lack of resolved hyperfine (hf) interaction and precise *g*-tensor measurements the so-called deep donor defects could not be identified. The only intrinsic defect clearly identified by magnetic resonance spectroscopy is the Ga interstitial [3]; it presents a very large central hf interaction which has been successfully modeled [24], whereas defects such as V_{Ga} , V_{N} , ($V_{\text{Ga}}-V_{\text{N}}$), and N_{int} have so far escaped clear identification. As ODMR measurements do not allow the determination of absolute defect concentrations their introduction rates could neither be established. Recent progress in the calculations of electronic and magnetic properties of intrinsic defects in GaN has given a new stimulus for such studies. It should be recalled that, as has been e.g. shown in the case of silicon carbide (SiC), intuitive models interpreting the hf interactions without extensive modeling can easily lead to erroneous assignments and are clearly insufficient [25–27]. Due to the high number of intrinsic defects which in addition may occur in several charge states, the situation is complex and theoretical support becomes a prerequisite for any defect identification. In GaN, the analysis of the hyperfine structure is not straightforward because of the presence of different

isotopes with nonzero nuclear spin—two Ga isotopes with nuclear spin $I = 3/2$ and comparable natural abundance, but different nuclear g factor, ^{69}Ga ($g_N = 1.344\,39$, 60.1%) and ^{71}Ga ($g_N = 1.708\,18$, 39.9%) and one nitrogen isotope ^{14}N with $I = 1$. In continuous wave (cw) EPR measurements, when hf interactions are resolved, this will lead to the superposition of Ga related quartet lines together with the triplet lines of the dominating nitrogen isotopes ^{14}N (99.7%, $I = 1$). But most often such multiple hf interactions lead to broadened lines without clearly resolved structure.

We have investigated very recently by electron paramagnetic resonance (EPR) spectroscopy and density functional theory (DFT) the defects introduced by high-energy particle irradiation in n -type GaN and found experimental evidence for a nitrogen sublattice related defect, the nitrogen split interstitial [28]. This configuration with two nitrogen atoms sharing a common nitrogen lattice site was predicted before by total energy and molecular dynamics calculations [20–23]. There was however no experimental evidence of this defect. Our recent EPR measurements in Ref. [28] confirm the theoretical predictions that single nitrogen interstitial atoms are not stable at tetrahedral or octahedral interstitial sites but form split interstitials, where two nitrogen atoms share a common N lattice site. Furthermore, the combined EPR and DFT investigations show that the bonding configuration of the N split interstitial depends strongly on the charge state and is temperature dependent. In Fig. 1 we illustrate the modeled low- and high-temperature configurations of the neutral $(\text{N-N})_{\text{N}}^0$ [28]. In this charge state this defect is paramagnetic with a spin $S = 1/2$; its point symmetry is very low: it changes from C_{1h}

for temperatures above 40 K to even C_1 for the low-temperature (LT) configuration.

In this work we have extended the previous study by combining electron paramagnetic resonance (EPR) with nuclear magnetic resonance and applying several magnetic resonance techniques *with increased resolution*: cw EPR at very high frequencies (up to 324 GHz) and Q -band electron nuclear double resonance (ENDOR), ENDOR induced EPR (EIE) and field-frequency ENDOR (FF-ENDOR [29]) spectroscopy.

Our experimental results are compared with theoretical predictions for all the ENDOR-relevant spectroscopical data including, besides the g tensors and hyperfine splitting, also the electric-field gradient (EFG) and the quadrupole coupling constants. By high frequency EPR we were able to (i) resolve the full g tensor confirming the theoretically predicted anisotropy, (ii) by Q -band ENDOR to observe for this defect hf interactions with distant Ga atoms, and last but not least (iii) by applying field-frequency (FF)-ENDOR to resolve the ENDOR spectra of the central N and Ga atoms predicted in the 20–90-MHz range. The special interest of the the FF-ENDOR technique is that it allows the detection of heavily broadened lines, buried in the noise when scanning at fixed magnetic field values.

II. EXPERIMENT

The GaN samples are commercially purchased freestanding c -axis oriented, n -type doped hydride vapor phase epitaxy (HVPE) grown films of typically 300 μm thickness. They were cut to $5 \times 5 \text{ mm}^2$ dimension with one of the axes parallel to the $(11\bar{2}0)$ direction. As the defect introduction depends on the mass and energy of the bombarding particles different types of irradiation conditions have been investigated: 20-MeV electrons, 12-MeV protons, and 120-MeV Si^+ ions. The maximum fluences were $2 \times 10^{18} \text{ cm}^{-2}$ (e^-), $8 \times 10^{16} \text{ cm}^{-2}$ (p^+), and $1 \times 10^{14} \text{ cm}^{-2}$ (Si^+). With increasing fluence of irradiation the samples became increasingly compensated and the Fermi level drops below the shallow effective mass (EM) donor level [30,31]. As the proton irradiation was found to have the highest introduction rate this case will be discussed here in particular. The high frequency (90–324 GHz) EPR measurements were made with a transmission-type spectrometer with a bolometer detector. Variable high frequencies are obtained by using frequency doublers and triplers starting from microwave sources in the 90-GHz range. The magnetic field was calibrated with the shallow donor resonance in GaN ($B||c$, $g = 1.952$). The Q -band ENDOR, EIE, and two-dimensional (2D) (FF)-ENDOR experiments were performed with a Bruker ELEXSYS E500 spectrometer. The spectra were measured at temperatures between 2 and 60 K. Different modulation frequencies between 180 Hz and 25 kHz have been applied. Most of the ENDOR spectra were obtained at $T = 6 \text{ K}$ with 12.5-kHz frequency modulation as for this condition the best signal-to-noise ratio was obtained. The simulations of the EPR and ENDOR spectra were performed with the EasySpin program [32].

III. COMPUTATION

In order to analyze the high frequency EPR and ENDOR results we have calculated all ENDOR relevant spectroscopical

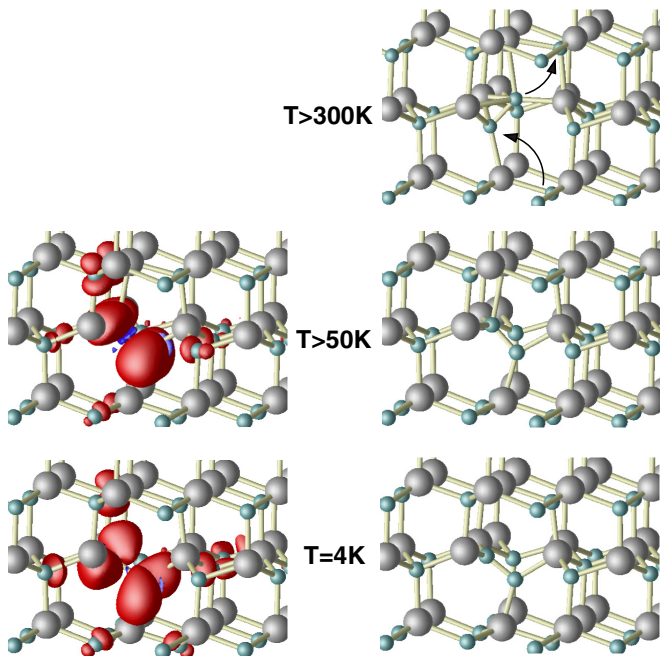


FIG. 1. (Color online) Low-temperature structure (LT, bottom) and high-temperature structure (HT within C_{1h} symmetry, middle) of the neutral nitrogen split interstitial. For a model of N diffusion, a possible migration path via an excited configuration (resembling the ground-state structure of the double positively charged state) is also indicated.

data for both the LT and HT configuration of the neutral N split interstitial: Besides the electronic g tensor and the hyperfine splittings, also the electric-field gradients (EFG) and quadrupole splittings are determined from first principles. The calculation of the defect structures as well as the spectroscopic ENDOR signatures for the N split interstitials were done in the framework of density functional theory. We use supercells containing 325 atoms, standard norm conserving pseudopotentials, a plane-wave basis with an energy cutoff of 90 Ryd (Ga $3d$ electrons in the valence), and the spin-polarized Perdew-Burke-Ernzerhof (PBE) functional [33]. All defect structures have been fully relaxed using $2 \times 2 \times 2$ Monkhorst Pack (MP) k -point samplings. The EPR/ENDOR parameters are calculated in scalar-relativistic approximation using the gauge-including projector augmented plane wave (GI-PAW) approach [34] as implemented in the QUANTUM-ESPRESSO package [35]. For the g -tensor calculation spin-orbit coupling is taken into account in linear magnetic response, whereby the deviation of the elements of the g tensor from the free-electron value 2.002 319 can be described in a physically meaningful way by the spin currents $\vec{j}(\vec{r})$ induced by the external magnetic field [24]. Note that at least $4 \times 4 \times 4$ k -point samplings are necessary to obtain well converged elements of the electronic g tensor.

The hyperfine (hf) splittings are determined by the magnetization density $m(\vec{r})$ —the probability of the unpaired electron—in a very small region around the nuclei [36]. Together with the g tensor these hf splittings can be directly compared with the experimentally resolved EPR parameters. In addition, we calculate the ENDOR frequencies for the nuclei within the defect structure from the nuclear Larmor frequency ν_L , the hyperfine splitting A , and the quadrupole splitting ν_Q for a given orientation of the magnetic field. The latter, the tensor of the quadrupole coupling, is related to the electrical-field gradient (EFG) $V_{ij} = \frac{\partial^2 V}{\partial X_i \partial X_j}$ by $\nu_Q = eq V_{ij}/2h$ where q is the nuclear quadrupole moment and h is the Planck constant. Since the defect under investigations shows a particular configurational anisotropy, the full tensors of all these quantities were determined in order to predict the ENDOR frequencies for a given orientation of the sample.

IV. EPR RESULTS AND DISCUSSION

A. X-band EPR

Before irradiation, the n -type doped samples display only the EPR spectrum of the neutral Si donor. After irradiation with a threshold fluence, for which the samples had become electrically compensated, an additional spectrum is observed. Its intensity increases linearly with the fluence. In Ref. [28] this spectrum was already assigned to the $(N-N)_N$ center. Typical X-band EPR spectra in the 4–20-K range are presented in Figs. 2 and 3. For fully compensated samples, only the spectrum of the N split interstitial is observed [Fig. 2(a)] whereas for less irradiated samples a weak donor line is still observed [Fig. 2(b)]. In this temperature range, the EPR spectrum of the N split interstitial has an overall width of 170 G and an average, effective g value of about 2.0014. The shallow donor line has a width of 10 G. For the orientation of the magnetic field parallel to the c axis the EPR spectrum of the N split interstitial

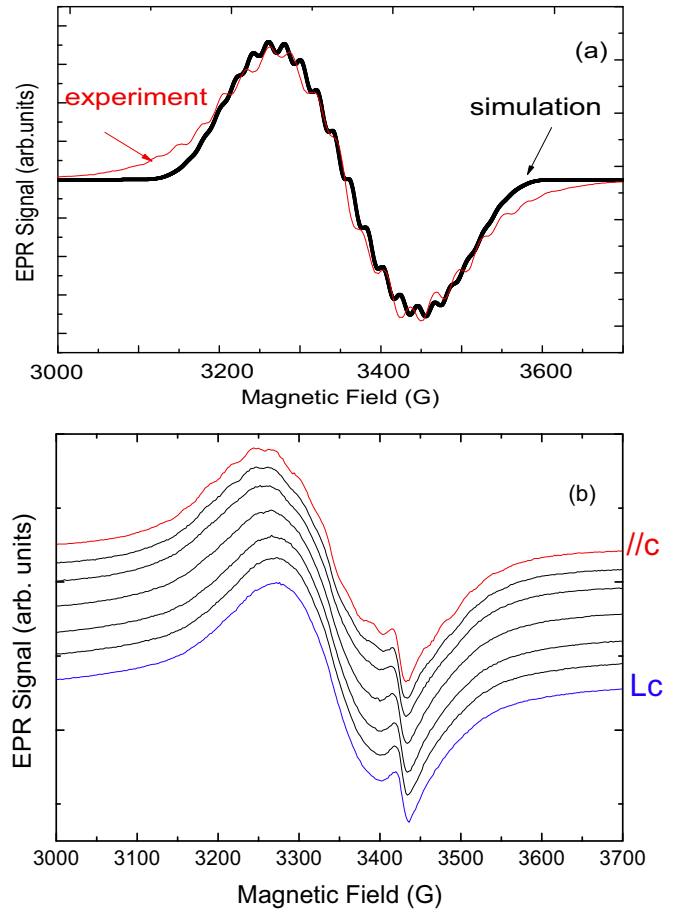


FIG. 2. (Color online) (a) Experimental X-band EPR spectrum (red), and the spectrum simulated based on the DFT prediction (black) of the $(N-N)^0$ defect for $B||c$ and $T = 4.2$ K; parameters are given in Table I. (b) Experimental angular variation of the $(N-N)^0$ EPR spectrum; $T = 4$ K, rotation axis $[1100]$.

shows a complex hf structure with an effective splitting of about 28 G [Fig. 2(a)]. This hf structure can be observed for orientations of the magnetic field up to 20° from the c axis [Fig. 2(b)] and then is broadened and becomes unobservable due to the superposition of different spectra from centers with the same microscopic configuration but different orientations. By rotating the samples from $B||c$ to $B \perp c$, the center of gravity of the spectrum shifts very slightly to higher fields. As shown in Fig. 2(a) the EPR spectrum shape and in particular its hf structure is well simulated with the DFT-predicted parameters of the neutral nitrogen split interstitial (see also Table I). In spite of its apparent simplicity the hf structure is complex and considering the local defect structure— $(Ga_2-N-N-Ga_2)$ with low symmetry—it results from the interaction with four nonequivalent Ga atoms and two nonequivalent N atoms. The multiplicity due to the presence of two Ga isotopes (^{69}Ga , ^{71}Ga) with nuclear abundances of 60% and 40% respectively has also to be taken into consideration. The full g tensor and ^{69}Ga hf interaction tensors for the low-temperature configuration of the neutral split interstitial with $S = 1/2$ and C_1 symmetry obtained by our modeling are given in Table I.

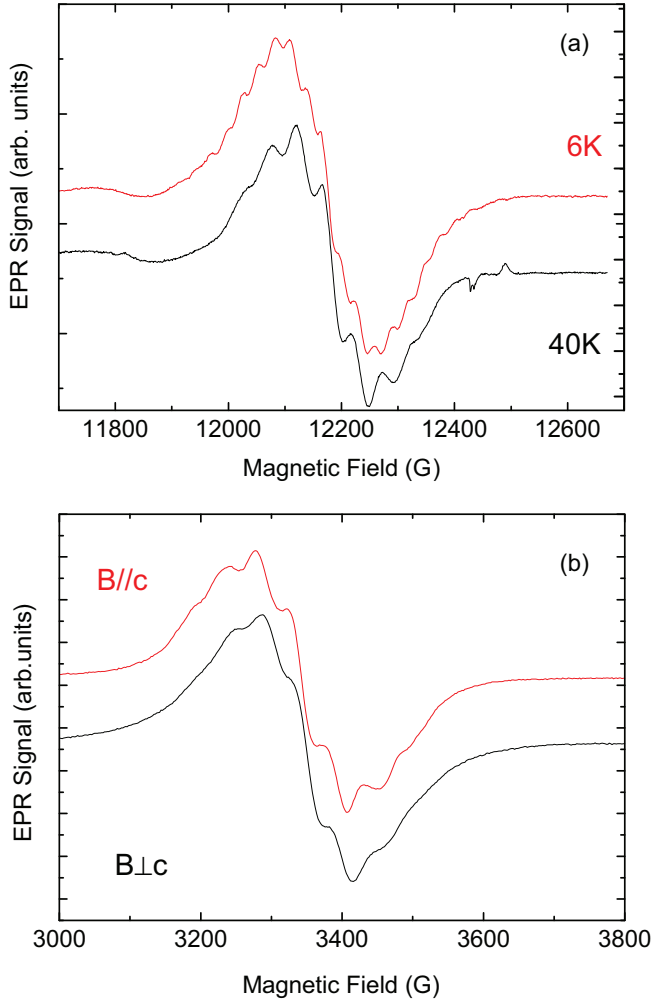


FIG. 3. (Color online) (a) Experimental Q -band EPR spectrum of the $(N-N)^0$ defect for $B||c$ recorded at $T = 6$ K (red) and 40 K (black); (b) X-band EPR spectrum of the $(N-N)^0$ center at $T = 40$ K for $B||c$ (red) and $B \perp c$ (black).

The N split interstitial can exist in different charge states depending on the Fermi-level position which will change with irradiation fluence. The following charge states can be observed in GaN: 2+, 1+, 0. In the 0 charge state it is

TABLE I. Calculated principal values and orientations of the low-temperature (ground state) g tensor of $(N-N)_N$ in the neutral and 2+ charge states. The measured data of the experimentally resolved spectrum are also given.

Model	Parameter	φ_{DFT}	ϑ_{DFT}	Value _{DFT}	ϑ_{exp}	Value _{exp}
$(N-N)_N^0$	g_{xx}	302	106.7	1.9966	113.7	1.9895
	g_{yy}	197	49.2	2.0016	42.6	2.0016
	g_{zz}	49	134.5	2.0036	134.5	2.0036
	$g_{ c}$		0.0	2.0016	0.0	2.0013
$(N-N)_N^{2+}$	g_{xx}	300	125.9	1.9727		
	g_{yy}	120	144.1	2.0015		
	g_{zz}	210	90.0	2.0024		
	$g_{ c}$		0.0	1.9868		

paramagnetic ($S = 1/2$), in the 1+ charge state this defect is diamagnetic ($S = 0$), and in the 2+ charge state it is again paramagnetic with a spin $S = 1/2$. Its charge state in a given sample will of course depend on the doping and the irradiation conditions. Using the gap-correcting HSE06 hybrid functional [37] we have previously [28] calculated the corresponding charge transition levels which are $E_C - 2.56$ eV, $E_C - 1.45$ eV, and $E_C - 1.01$ eV corresponding to the $+/2+$, $0/+$, and $-/0$ transitions respectively. From *in situ* photo EPR measurements, showing a threshold energy of 1.0 eV, we had deduced that the Fermi level becomes pinned at the $(-/0)$ transition for high fluences; thus we observe by EPR the neutral charge state [28].

We have equally calculated the g tensor for the 2+ charge state. Its g tensor, especially the orientations, is quite different which allows us to discriminate between the two cases. Indeed, for an orientation of the magnetic field $B||c$, for which the magnetically nonequivalent centers will superpose at the same resonance field (equivalent to $g_{||c} = 2.0013$), we expect an effective g factor of $g_{||c} = 2.0016$ for the neutral center whereas for the 2+ charged center our DFT modeling predicts a much smaller value of $g_{||c} = 1.9868$.

In X- and Q-band EPR at temperatures above $T = 40$ K the hf structure of the defect is observed to change; the splitting increases, the multiplicity decreases, and the structure becomes more isotropic [Fig. 3(b)]. The hf structure can be described by an effective hf splitting of 126 MHz (42 G). Since the single positive charge state is diamagnetic and since the 2+ charge state provides again a much too small g value for $B||c$, a simple Fermi-level effect, i.e., a thermal shift of the Fermi level towards midgap, has to be ruled out. Such a change in the EPR spectra is however often observed for defects in semiconductors such as SiC and may correspond to a thermally activated reorientation or a change in the bonding configuration. In this high-temperature configuration the symmetry of the defect changes to C_{1h} . This temperature-dependent transformation has equally been modeled within DFT. However, in contrast to the low-temperature configuration which is simply given by the overall ground-state configuration of the neutral N split interstitial, the description of the HT state is less straightforward. The change in the spectra can either be explained by a dynamical Jahn-Teller effect resulting in a motional averaged defect orientation or by a transition to a close-by local minimum which is separated from the LT ground state by an extremely low-energy barrier. Experimentally, we were not able to discriminate between these two possibilities. According to our total-energy calculation, however, the energy barrier for such a transition is indeed very low: a Fermi-Dirac-like occupation of the band-structure equivalent to about 80 K is sufficient to yield a defect configuration with higher symmetry, C_{1h} . It thus appears reasonable to use the resulting state as an estimate for the experimental situation which gives rise to the HT spectra. The resulting HT values for the g and hf (A) tensors of this center are compiled in Table III and can nicely explain the observed temperature induced change of the EPR spectrum: Within the C_1 ground-state configuration, the unpaired electron giving rise to the EPR signature is mainly localized in the p -like orbitals of the two central N atoms. The resulting magnetization density $m(\vec{r})$ resembles a four-leaf clover which

TABLE II. Calculated ^{69}Ga and ^{14}N hf interaction tensors of the $(\text{N-N})^0$ center at low temperature; values are given in MHz. To obtain ^{71}Ga hf interactions the given data have to be multiplied by $1.708\ 18/1.344\ 39 = 1.2706$.

Nuclei	Parameter	φ_{DFT}	ϑ_{DFT}	Value _{DFT}	ϑ_{exp}	Value _{exp}
^{14}N	A_{xx}	299	126.1	9.3		
	A_{yy}	167	132.4	9.7		
	A_{zz}	250	116.4	74.2		
	$A_{ c}$		0.0	22.3	0.0	15
^{14}N	A_{xx}	299	125.8	10.3		
	A_{yy}	190	114.3	10.7		
	A_{zz}	74	134.3	76.5		
	$A_{ c}$		0.0	42.7	0.0	42
^{69}Ga	A_{xx}	32	110.2	78.1		
	A_{yy}	299	99.0	80.5		
	A_{zz}	186	157.7	120.3		
	$A_{ c}$		0.0	114.3	0.0	116
^{69}Ga	A_{xx}	38	90.6	75.5		
	A_{yy}	136	167.8	76.9		
	A_{zz}	228	102.2	111.4		
	$A_{ c}$		0.0	82.0	0.0	92
^{69}Ga	A_{xx}	89	109.9	40.2		
	A_{yy}	187	159.6	41.7		
	A_{zz}	4	94.3	65.6		
	$A_{ c}$		0.0	41.7	0.0	65
^{69}Ga	A_{xx}	18	135.0	54.1		
	A_{yy}	243	125.4	55.8		
	A_{zz}	134	113.9	85.1		
	$A_{ c}$		0.0	59.7	0.0	75

is tilted with respect to the crystal axes (cf. Fig. 1). In this LT configuration the magnetization is distributed equally to the two central N atoms (cf. the principle hf values A_{xx} , A_{yy} , A_{zz} in Tables II and III). This tilted ground-state geometry can be rationalized by noting that thereby the minimal angle between the clover leaves plane and the bonding between the four Ga ligands is maximized. Obviously a tilted structure with lower C_1 symmetry is energetically more favorable than destroying the planar coupling of the p orbitals and realizing a more symmetric magnetization density with, e.g., two perpendicular p orbitals. In this sense, it is the strong planar coupling of the two p -like orbitals into a clover leaf that is the basic ingredient of the neutral N split interstitial. As a result of the average positioning of the clover leaf, the hf splittings due to the four Ga ligands are comparable and do not differ by more than a factor of 2. A slightly different orientation of the principle axes of the two quasiequivalent N atoms, however, leads to clearly distinct splittings if the magnetic field is applied parallel to the hexagonal c axis (15 vs 42 MHz). Within the thermally averaged configuration, however, the clover leaf is oriented perpendicular to a $(11\bar{2}0)$ mirror plane of the crystal retaining C_{1h} symmetry. Thereby, the distance between the two central N atoms is slightly reduced. More important, the orientation of the p -like orbitals with respect to the direct ligands changes completely. The p -like orbital at the N atom between the two nonequivalent Ga ligands located within the $(11\bar{2}0)$ is oriented perpendicular to the mirror plane, and resembles a free p -orbital, i.e., the orbital becomes more polarized with an

TABLE III. Calculated high-temperature g tensor and hf tensors (MHz) of the $(\text{N-N})_N^0$ center (principal values and orientations of the principal axes). The experimental data measured at 40 K are also given.

Nuclei	Parameter	φ_{DFT}	ϑ_{DFT}	Value _{DFT}	ϑ_{exp}	Value _{exp}
	g_{xx}	300	114.5	2.0006		
	g_{yy}	120	55.5	2.0015		
	g_{zz}	30	90.0	2.0021		
	$g_{ c}$		0.0	2.0009	0.0	2.0005
^{14}N	A_{xx}	300	133.2	14.0		
	A_{yy}	120	136.8	21.1		
	A_{zz}	210	90.0	92.2		
	$A_{ c}$		0.0	17.8	0.0	30
^{14}N	A_{xx}	300	133.1	4.5		
	A_{yy}	120	136.9	21.2		
	A_{zz}	30	90.0	33.4		
	$A_{ c}$		0.0	13.4	0.0	10
^{69}Ga	A_{xx}	300	106.2	-25.1		
	A_{yy}	30	90.0	-20.4		
	A_{zz}	120	163.8	-14.1		
	$A_{ c}$		0.0	-14.9	0.0	<25
^{69}Ga	A_{xx}	94	90.6	125.8		
	A_{yy}	187	167.8	125.9		
	A_{zz}	4	102.2	177.5		
	$A_{ c}$		0.0	128.2	0.0	110
^{69}Ga	A_{xx}	146	90.6	125.8		
	A_{yy}	53	167.8	125.9		
	A_{zz}	236	102.2	177.5		
	$A_{ c}$		0.0	128.2	0.0	110
^{69}Ga	A_{xx}	300	158.8	-27.7		
	A_{yy}	210	90.0	-26.7		
	A_{zz}	120	111.2	-18.2		
	$A_{ c}$		0.0	-26.4	0.0	<25

increased anisotropic character. Its Ga ligands are less affected by the unpaired electron and show a reduced hf splitting below 25 MHz. The situation at the other half of the defect is vice versa: the p orbital is aligned along the bond direction of the neighboring equivalent Ga ligands. A large amount of the magnetization is transferred to these Ga ligands, giving rise to a much smaller hf splitting due to the N nucleus and considerably increased, but still comparatively isotropic hf values due to the two equivalent Ga ligands. A value of 128 MHz for $B_{||c}$ nicely explains the experimental observation of an effective splitting of 126 MHz, whereby the reduction of the number of dominating Ga ligands from four inequivalent to two equivalent simplifies the superposition of the EPR pattern. As a result, the hf splitting due to the Ga ligands can now be resolved for all orientations.

B. 35 and 324 GHz EPR

We have measured the same samples at 35 GHz [Fig. 3(a)] and 324 GHz (Fig. 4). Measuring at higher frequencies increases the resolution of EPR spectra composed of g -tensor split multiple lines. It is also useful to verify whether more than one defect is contributing to the overall EPR spectrum. It is instructive to note here that such a superposition

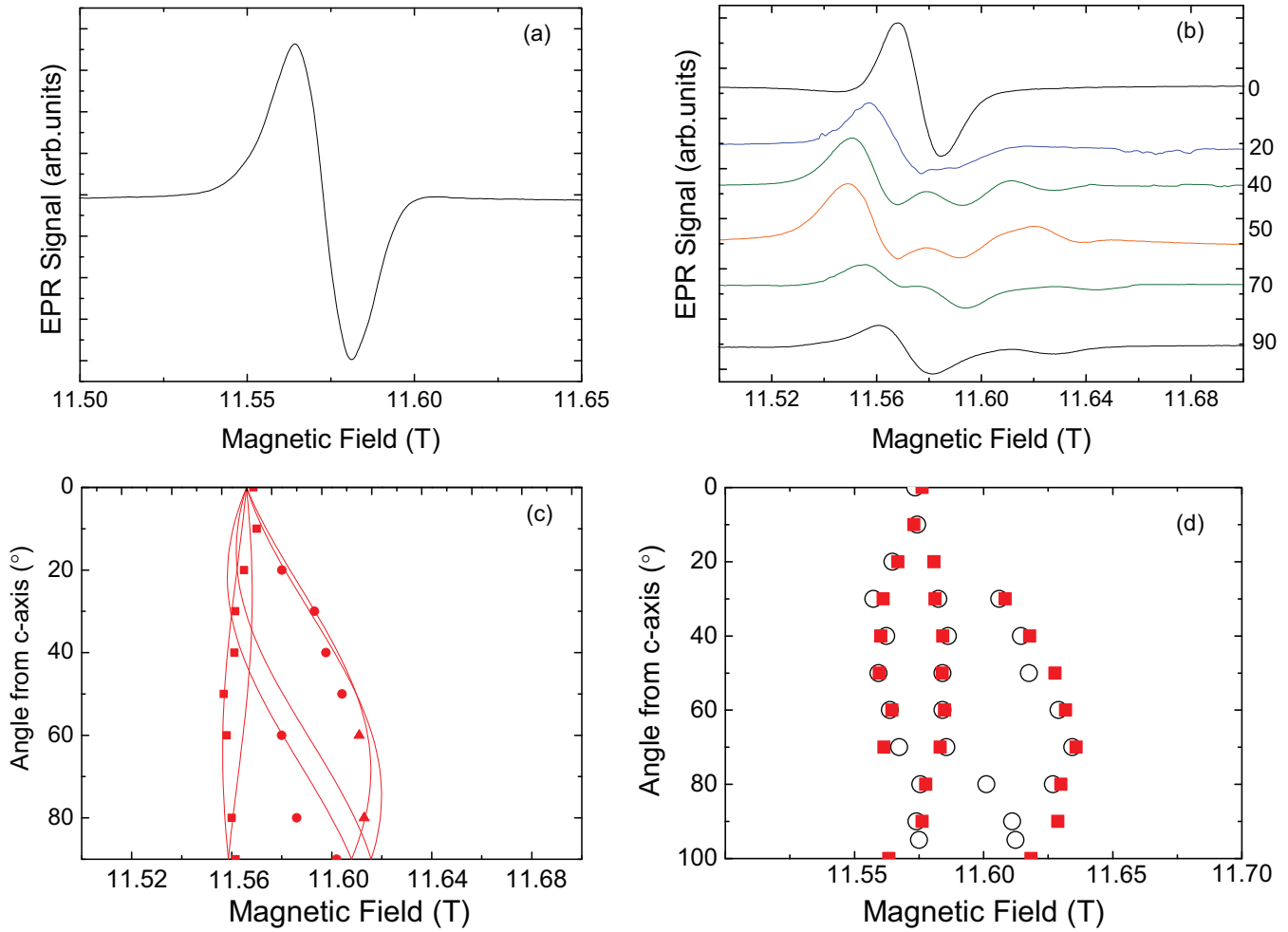


FIG. 4. (Color online) (a) 324-GHz EPR spectrum of $(N-N)_N^0$ at $T = 10$ K, $B \parallel c$. (b) Angular variation of the $(N-N)_N^0$ spectrum at $T = 6$ K. (c) Predicted angular variation of the $(N-N)_N^0$ spectrum in two rotation planes $(1\bar{1}00)$ (red line) and $(11\bar{2}0)$ (black line); experimental results (red circles). Values are explicitly given in the upper right corner. (d) Experimental angular variation of the EPR spectra between $B \parallel c$ and $B \perp c$ at $T = 10$ K (red squares) and $T = 60$ K (black circles).

of spectra was recently proposed to explain a similar EPR pattern in GaN [8]. The line shape of the EPR spectrum is not modified between X -band and Q -band measurements which indicates that the spectrum belongs to one defect only. Thus, we have undertaken additional EPR measurements at still higher microwave frequencies up to 324 GHz. In Figs. 4(a) and 4(b) we show the 324-GHz EPR spectra of a fully compensated sample. In the field region of $g = 2$ which occurs at 11.6 T we observe only the spectrum of the $(N-N)_N$ defect. The overall linewidth is not increased relative to the X -band measurements (Fig. 5). This excludes definitely the possibility that the EPR spectrum of another defect is superposed on the $(N-N)_N$ spectrum in our samples, which might have perturbed the X -band EPR spectrum simulations. The g -tensor anisotropy is now partially resolved in such a way that a determination of the full g tensor becomes possible. We have measured [Figs. 4(c) and 4(d)] the angular variations of the EPR spectra in two rotation planes $(1\bar{1}00)$ and $(11\bar{2}0)$ and determined the principal values of the g tensor. The hf structure of 2.8 mT for $B \parallel c$ is no longer resolved at this frequency due to an insufficient field resolution at fields of 12 T. The values obtained are very close to the theoretically predicted

values: $g_{xx} = 1.9985$; $g_{yy} = 2.0016$; $g_{zz} = 2.0036$ (experiment), cf. Table I; $g_{xx} = 1.9966$; $g_{yy} = 2.0016$; $g_{zz} = 2.0036$ (theory).

We have also measured the high-temperature configuration of this defect at 324 GHz. As shown in Fig. 4(d), we observe at $T = 60$ K a g -tensor anisotropy with principal values close to those observed at 6 K; thus at this frequency the high-symmetry configuration is not yet detectable at 60 K. In Fig. 5 we directly compare the line shape of the $(N-N)_N^0$ center for $B \parallel c$ and $T = 6$ K measured at 9.5-, 35-, 324-GHz EPR frequencies. The resonance field has been set to zero for the three spectra and the spectra are displayed on the same magnetic field scale. Remarkably the linewidth and line shape do not change in this large frequency range.

V. ENDOR MEASUREMENTS

For an unambiguous, conclusive proof of the N split interstitial configuration via its hf structure, ENDOR is a suitable technique since it gives access to the central and ligand hf interaction parameters modeled by us. It allows us further to determine directly the atomic species via the field/frequency

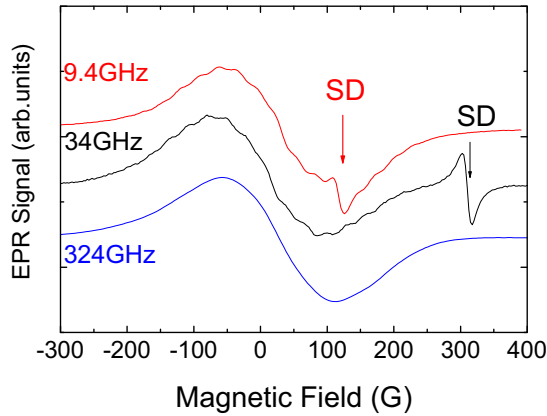


FIG. 5. (Color online) Comparison of the $(N-N)_0$ EPR spectra for $B||c$ at $T = 4$ K measured at X band (red), Q band (black), and 324 GHz (blue). The resonance from the shallow donor (SD) is also indicated. In the case of 324 GHz it is outside the B -field range with respect to the resonance center of gravity.

shifts of the ENDOR lines. Previously, ENDOR measurements on the shallow donor in GaN have been already attempted with optically (photoluminescence) detected ENDOR at K -band and Q -band frequencies [38,39]. Due to the delocalized wave function of the EM donor, only Larmor spectra of distant nuclei can be expected. Two broad (400 kHz) Ga ENDOR lines were observed, however, their quadrupole splitting was not resolved; no N-related ENDOR line could be observed. So far, no ENDOR spectrum could be observed for any deep donor center in GaN. We have performed ENDOR measurements at 35 GHz on the $(N-N)_N^0$ center. At this frequency the EPR resonance field of the $(N-N)_N^0$ center is close to 12.2 kG. In principle one can expect for this deep center the observation of three types of ENDOR spectra corresponding to interactions with (i) very distant N and Ga nuclei, (ii) with weakly interacting nuclei, and (iii) strongly interacting close neighbor atoms. All lines will be further split by quadrupole interactions due to the nuclear spin $I \geq 1$ of ^{14}N ($I = 1$) and ^{69}Ga and ^{71}Ga (both with $I = 3/2$): At a magnetic field of about 12 kG the nuclear Larmor lines of the *distant* ^{14}N , ^{69}Ga , and ^{71}Ga nuclei are expected at frequencies of 3.8, 12.8, and 15.8 MHz respectively. Nuclei with weak hf interaction will give rise to a set of lines with ENDOR frequencies of $\nu_L \pm A/2$ further split by the quadrupole interaction. The nuclei with strong hf interaction will introduce pairs of quadrupole split triplet ($^{69}\text{Ga}/^{71}\text{Ga}$) or doublet (^{14}N) spectra at frequencies $A/2 \pm \nu_L$, resulting in ENDOR frequencies $A/2 \pm (\nu_L + m_q \cdot \nu_Q)$ with $m_q = 0, \pm 1$. Both partially compensated samples showing in addition a weak shallow donor line and fully compensated samples have been studied. At this frequency, the resonance positions of the two lines are separated by 300 G. The exclusive correlation of the ENDOR spectrum with the $(N-N)_N$ EPR spectrum has been verified by ENDOR induced EPR.

A. ENDOR lines of distant nuclei

As shown in Figs. 6(a) and 6(b) we observe various well-resolved ENDOR lines in the frequency range 10–20 MHz.

We also searched for ENDOR lines in the 1–10-MHz range as the nitrogen Larmor lines are expected at 3.8 MHz; no such lines could be detected. The strongest lines in the 10–20-MHz range can be attributed to ENDOR with distant Ga nuclei. Their spectra are composed of two triplets centered at 12.4 and 15.8 MHz corresponding to the quadrupole interaction split Larmor spectra of the ^{69}Ga and ^{71}Ga nuclei. Both nuclei have spin $I = 3/2$ but different magnetic moments and different electric quadrupole moments. The attribution to Ga nuclei was further confirmed by the measurement of the field/frequency shift when the EPR field position was shifted through the $(N-N)_N$ EPR line. The linewidth of the central ($m_q = 0$) Ga ENDOR lines is 0.32 MHz. The linewidth of the $m_q = \pm 1$ quadrupole split lines are larger—0.51 MHz—as these lines are sensitive to the strain present in the HVPE grown layers. The quadrupole splitting and the angular variation of the distant ENDOR lines can be described with the following spin Hamiltonian:

$$H_n = \sum_{i=1}^3 (-g_{n,i} \beta_n I_i B + I_i Q_i I_i), \quad (1)$$

where the sum runs over the nuclei with nonvanishing magnetic moment, $^{69}\text{Ga}/^{71}\text{Ga}$ and ^{14}N . The first term in brackets represents the nuclear Zeeman energy and the second accounts for the quadrupole interaction energy. Q_i is the quadrupole tensor, which is axial in the case of the ideal GaN wurtzite crystal structure. The quadrupole coupling constant is related to the electrical field gradient (EFG) $V_{zz} = \frac{\partial^2 V}{\partial z^2}$ along the hexagonal c axis by $\nu_Q = eq V_{zz}/2h$ where q is the nuclear quadrupole moment and h is the Planck constant. The splitting follows a simple $(3 \cos^2 \theta - 1)$ angular dependence when the asymmetry parameter is zero. The quadrupole coupling constant and the electric field gradients at the Ga nuclei sites can be directly deduced from the $B||c$ ENDOR spectrum. We obtain values of $\nu_Q(^{69}\text{Ga}) = 1.33$ MHz and $\nu_Q(^{71}\text{Ga}) = 0.85$ MHz. Alternatively, the second-order shift of the central quadrupole line of the ^{69}Ga nucleus can be used to deduce the quadrupole coupling constant. Following Ref. [40] the maximum relative shift of the central line for a rotation of the magnetic field between $||c$ and $\perp c$ is given by $\Delta\nu = 33/64 \nu_Q^2/\nu_L$, with ν_L the Larmor frequency. From the observed maximum shift of $\Delta\nu = 70$ kHz for the ^{69}Ga line [cf. Fig. 6(d)] we deduce a coupling constant of 1.30 MHz which is within the error limits in good agreement with the value deduced from the angular variation of the quadrupole lines. These values agree also with those previously published for as-grown materials of different origin [38,40–43]; see also Table IV.

B. ENDOR lines of strongly interacting nuclei

Whereas the width of the Larmor lines and the corresponding quadrupole splitting factors of distant nuclei are of interest for the characterization of the GaN material they do not inform us on the defect model. This information, however, is hidden in the ENDOR lines of nuclei strongly interacting with the defect center.

The ENDOR spectra were modeled with the EasySpin program [32] in the perturbation approximation. The ENDOR

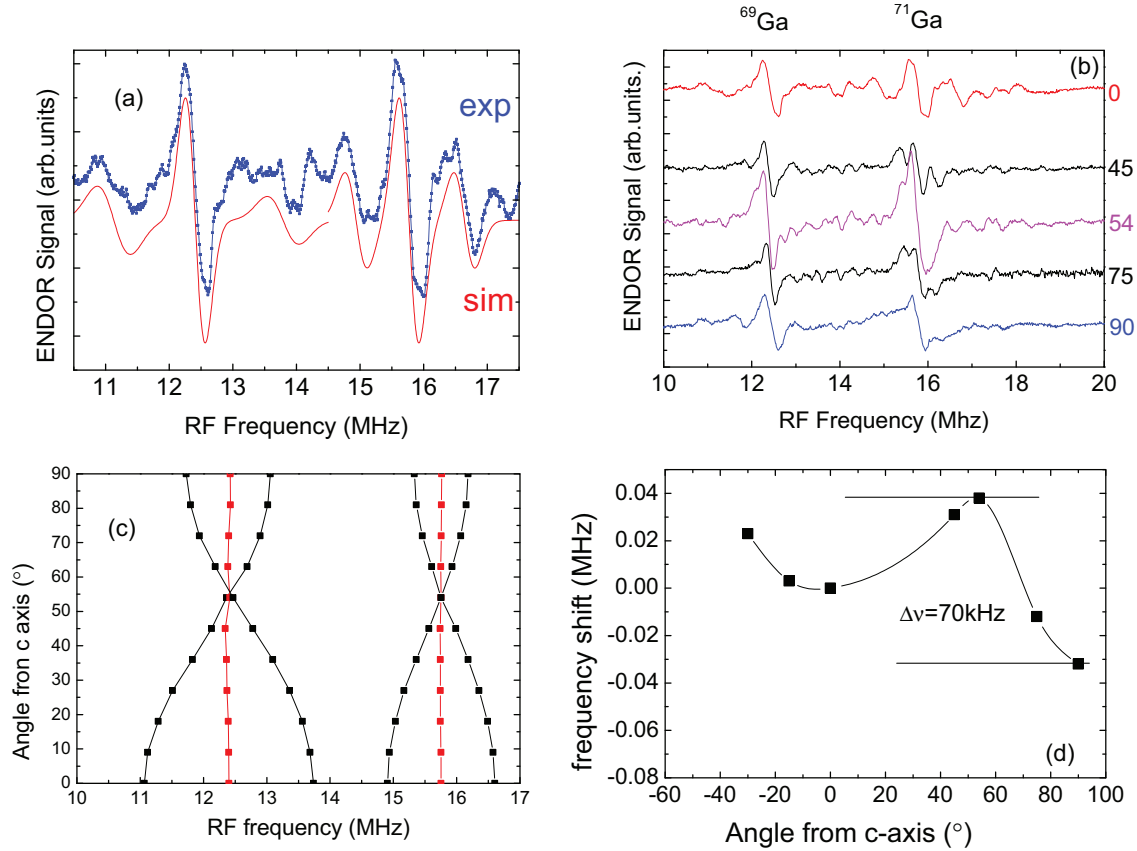


FIG. 6. (Color online) (a) Q -band ENDOR spectrum of the $(N-N)^0$ center (blue points) and its simulation by Gaussian lines (red line); $T = 6$ K and $B||c$. (b) Angular variation of the ENDOR spectra of the ^{69}Ga , ^{71}Ga quadrupole interaction split Larmor lines. (c) Angular variation of the quadrupole interaction split Larmor lines of ^{69}Ga and ^{71}Ga . (d) Angular variation of the central ($m_I = 0$) ^{71}Ga Larmor line.

spectra of the strongly interacting nuclei will be composed of those of the two central N and four nearest Ga neighbor atoms. We have further to consider the isotope distribution and thus they were obtained as the weighted sum of the spectra of the 16 different isotope combinations $^{69-71}\text{Ga}$ of the four nonequivalent Ga neighbors and the two N central atoms. The

relative weights are deduced from the isotopic abundances of 60.1% (^{69}Ga) and 39.9% (^{71}Ga). In the general case when a paramagnetic electronic structure with total spin $S = 1/2$ interacts with the six nuclei as given in the local structure ($\text{Ga}_2\text{-N-N-Ga}_2$) the Hamiltonian H is given by

$$H = \beta S g B + \sum_{i=1}^6 (S A_i I_i + I_i Q_i I_i - g_{n,i} \beta_n I_i B). \quad (2)$$

In a first approximation, valid to second order, we treated each pair electron nucleus in an independent way, which neglects the pseudodipolar interactions between the nuclei. Within this model we can directly predict the ENDOR transitions for $B||c$ based on the calculated hf interactions parameters for the $(N-N)_N^0$ center via $A/2 \pm \nu_L$. The resulting values are compiled in Table VI. As we have neglected the quadrupole splitting at the defect site, the calculated line positions correspond to the central ($m_q = 0$) ENDOR lines. The quadruple splitting is indirectly taken into account by assuming a line width broadening of a few MHz.

To get more information about the quadrupole splitting of the central nuclei, we calculated these values from first principles using linear magnetic response for the neutral and 2+ charge state of the $(N-N)_N$. First, in order to evaluate the theoretical method, we apply the GIPAW code of the QUANTUM ESPRESSO package to calculate the EFG and quadrupole splittings of the ideal crystal. The calculated values are in

TABLE IV. Quadrupole coupling constants and EFG data for distant nuclei. Calculated values for ideal bulk 2H-GaN as well as for a neutral/ionized Si_{Ga} donor (weighted average of a 324 atomic supercell) in comparison with experimental data, (a) from this work (300- μm -thick HVPE grown layer) and (b) from NMR Ref. [40]. The coupling constants ν_Q are in MHz, and the EFGs (V_{zz}) in units of 10^{20} V/m².

Model, doped material	^{69}Ga		^{71}Ga		^{14}N	
	V_{zz}	ν_Q	V_{zz}	ν_Q	V_{zz}	ν_Q
Theory						
Ideal crystal	7.17	1.44	7.17	0.98	0.59	0.02
Si_{Ga}^+	6.78	1.36	6.78	0.92	0.56	0.02
Si_{Ga}^0	6.50	1.31	6.50	0.88	0.55	0.02
Experiment						
(b) highly resistive	6.77	1.38	6.88	0.88		
(b) $10^{19}\text{-}10^{20}\text{cm}^{-3}$	6.65	1.35	6.72	0.86		
(a) this work		1.33		0.85		

TABLE V. Quadrupole coupling constants and EFG (localized contributions) of the NN split interstitial for ^{14}N and ^{69}Ga : To obtain the values for ^{71}Ga the given ^{69}Ga values have to be multiplied with $11.7/17.1 = 0.626$. The maximum coupling constants ν_Q are in MHz, and the corresponding EFGs, V_{zz} , in units of 10^{20} V/m 2 ; their anisotropy is described by $\eta = (V_{xx} - V_{yy})/V_{zz}$, whereby z denotes the principal axis of the quadrupole tensor for a given nucleus. Its orientation (angle ϑ) with respect to the c axis of the hexagonal GaN crystal is also given. Along the c axis the smaller quadrupole splittings $\nu_{Q\parallel}$ are expected.

Nucleus	$(\text{N-N})_{\text{N}}^{2+}$					$(\text{N-N})_{\text{N}}^0$					$(\text{N-N})_{\text{N}}^0$ HT				
	$\nu_{Q\parallel}$	ν_Q	V_{zz}	η	ϑ	$\nu_{Q\parallel}$	ν_Q	LT V_{zz}	η	ϑ	$\nu_{Q\parallel}$	ν_Q	V_{zz}	η	ϑ
N1	1.10	-1.90	-79.13	0.387	145	0.49	-2.07	-86.52	0.461	114	0.17	1.25	52.24	0.667	137
N2	1.07	-1.89	-79.06	0.168	146	-0.21	-1.94	-81.19	0.442	131	-0.33	-2.08	-87.03	0.601	137
Ga1	43.54	43.55	216.81	0.071	179	4.08	-9.18	-45.74	0.894	117	3.67	-7.60	-37.87	0.908	119
Ga2	-9.12	32.09	159.75	0.094	111	4.44	11.13	55.45	0.189	139	0.47	11.80	58.77	0.175	129
Ga3	-9.12	32.09	159.75	0.095	111	-1.88	9.93	49.45	0.146	116	0.47	11.80	58.77	0.175	129
Ga4	-11.98	42.61	212.14	0.131	109	-1.60	10.58	52.67	0.101	116	-2.89	11.52	57.39	0.047	113

reasonable agreement with previous experimental data (see Table IV). Especially the values for the highly resistive material agree very well with the value obtained for the Si_{Ga}^+ case. The fact that for n -type conductive material slightly lower values are observed agrees with the measured values shown in Table IV. This trend is corroborated by additional calculations in which we investigate the influence of Si donors (in both neutral Si_{Ga}^0 and ionized form Si_{Ga}^+) whereby the donor is modeled in a 324-atom containing supercell. To obtain an estimate for the quadrupole interaction of distant nuclei we calculate an average of those nuclei which are more than 5 Å away from the Si donor atom. The atoms close to the donor atom are left out to exclude the influence of local strain. As a consequence, the remaining effect—the shift of the EFG and the quadrupole interaction to slightly smaller values—can be attributed to an increase of global strain within the supercell. Moreover, the DFT-calculated quadrupole splittings show that the quadrupole splitting of the N-related Larmor lines will not be observable for typical line width of 400 kHz: the EFG at the N nuclei is by a factor of 3 smaller than for the Ga nuclei and given the much smaller atomic quadrupole moment this gives rise to quadrupole splittings of 200 kHz.

Motivated by the success of our theoretical modeling in the case of ideal and Si-doped GaN crystals, we apply the same method for calculating the quadrupole splitting for different configurations of the N split interstitial, the low-temperature as well as high-temperature configuration of the neutral defect and, in addition, the ground state of the 2+ charge state. For the nuclei in the defect center we obtain exceptionally anisotropic quadrupole tensors, which—depending on the orientation—can change sign and give rise to quadrupole splittings of up to 2 MHz and up to 90 MHz for the two N atoms and the four Ga ligands, respectively (cf. Table V). According to our calculations in the 2+ charge state of the split interstitial one of the Ga ligands (Ga1) would have a very large quadrupole splitting of 43.5 MHz if the magnetic field is applied parallel to the hexagonal c axis of the GaN crystal. The other three ligands give rise to negative, but still comparatively large, splittings of about -9 MHz. The neutral charge state however, provides a special orientation of the central N-N dimer characterized by an average positioning (cf. the discussion in Sec. IV A), for which the quadrupole splitting for $B\parallel c$ of all four Ga ligands is reduced to smaller values of about 4.2 MHz (Ga1, Ga2) and -1.8 MHz (Ga3,

Ga4). Hence, based on the calculated Ga-related quadrupole splittings we are able to clearly distinguish between the neutral and 2+ charge state of the N split interstitial, and—as will be shown below—to confirm our assignment to the neutral charge state.

VI. FF ENDOR—STRONG HF INTERACTIONS

As no well resolved ENDOR lines could be observed in the 20–100-MHz range where, according to our modeling and EPR results, the ENDOR lines related to the hf interactions with the Ga nearest neighbors are expected, we have performed FF-ENDOR [38] measurements for two main orientations of the magnetic field $B\parallel c$ and $B \perp c$. The interest of FF-ENDOR is that it allows the observation of heavily broadened lines, difficult to detect by scans at a fixed magnetic field value. We scanned the magnetic field in small steps of 5 G over the EPR line and measured at each field the corresponding ENDOR spectrum. The result is shown in a 2D intensity color plot [Figs. 7(a)–7(d)] with the rf frequency as abscissa and the applied magnetic field as ordinate. Frequency modulation is used whereby first derivative Gaussian line shapes are expected. Horizontal cuts correspond to an ENDOR spectrum at a given magnetic field position whereas slightly inclined vertical cuts correspond to ENDOR induced EPR spectra at a specific ENDOR line. The field/frequency (FF) shift of the nuclei will give rise to characteristic inclination of the ENDOR spectra if isolated low or high frequency lines can be observed. In that case the field shift allows their association to a specific nucleus.

We clearly observe ENDOR transitions in the 20–90-MHz range. As expected, the lines are heavily broadened as compared to the Larmor lines. The origin of the severe line broadening is certainly short electronic relaxation times—a consequence of the high defect concentration necessary for ENDOR spectroscopy. To allow a better comparison with the predicted ENDOR lines in the $(\text{N-N})_{\text{N}}^0$ model we have extracted ENDOR spectra from the 2D field/frequency (FF) plots, by horizontal cuts and averaging over a vertical 30-G range. The results are shown in Fig. 8 and compared with a theoretical ENDOR spectrum simulated with the EASYSYSPIN program using the predicted ENDOR frequencies (shown in Table VI) and assuming a constant linewidth of 1 MHz. High frequency transitions are indicated by bold sticks and the low frequency transitions by light sticks. For $B\parallel c$ we experimentally observe

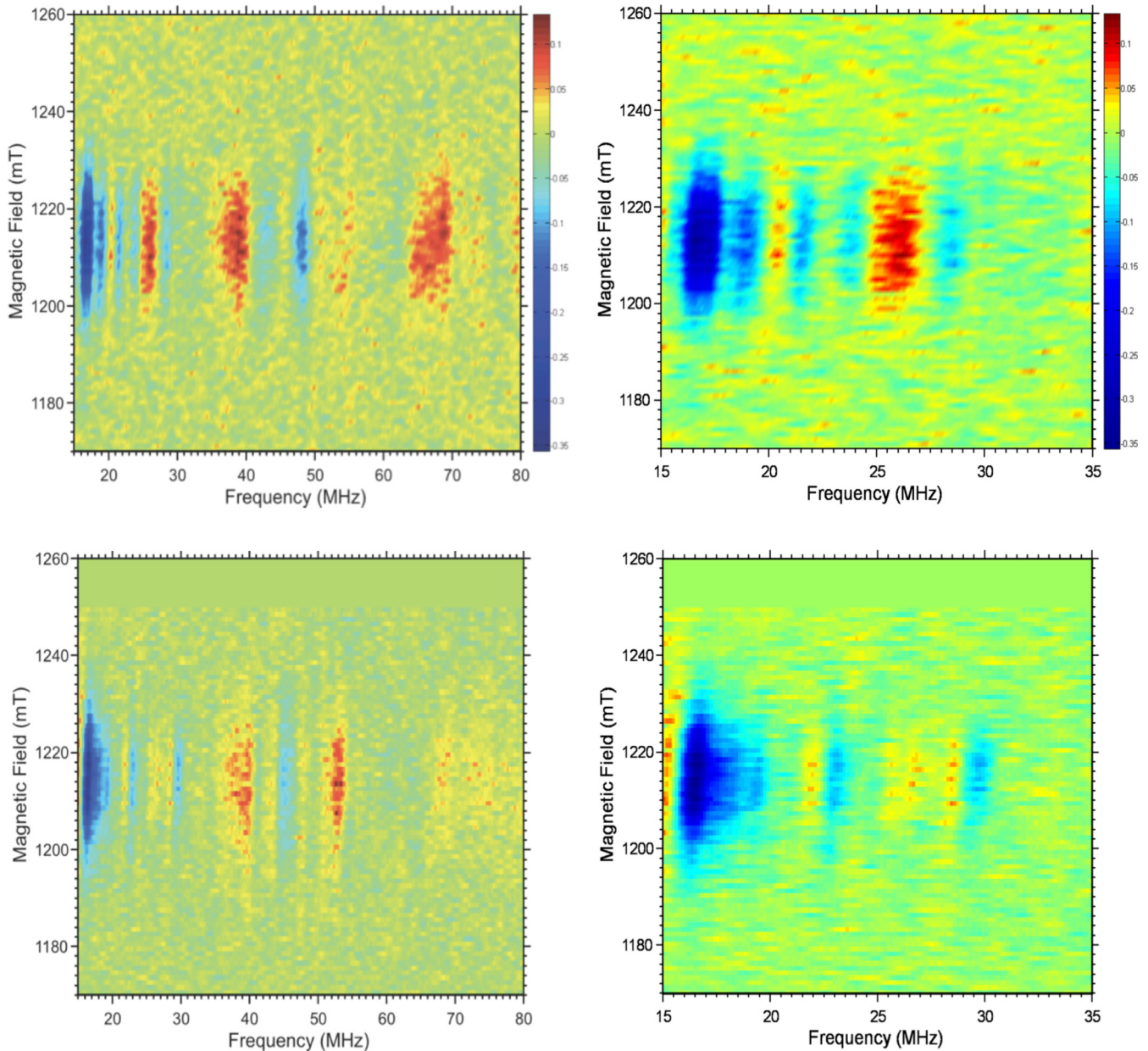


FIG. 7. (Color online) (a) FF ENDOR spectrum for $B \parallel c$ at $T = 6$ K; (b) zoom of the lower frequency part; (c) FF ENDOR spectrum for $B \perp c$ at $T = 6$ K; (d) zoom of the lower frequency part.

ENDOR intensities at 17, 25, 38, 48, and 68 MHz [cf. Figs. 7(a)–7(d)]. Thereby, the predicted high frequency N-related ENDOR line at 24.8 MHz is compatible with our experimental results [Fig. 8(a)] as the spectrum simulation with the EASYSIM program reveals its low intensity [Fig. 8(b)] compared to the Ga-related lines. The low-field counterpart at 17.2 MHz is superposed by the intense Lamor line. In the 30–90-MHz we observe—as expected—only Ga isotope related ENDOR transitions. A clear Ga related field/frequency shift is visible in the 40- and 68-MHz range where the high frequency lines of the two Ga isotopes are superposed. At first view, the predicted transitions at 54 and 58 MHz seem to be absent in the experiment. A look at the FF-ENDOR spectra in Fig. 7(a) shows, however, that at least the 54-MHz transition can be found at some values for the magnetic field. In the

EASYSIM program the quadrupole splitting could not be included; this is expected to lead to additional broadening of the spectra. In addition, the estimated error of the calculated ENDOR frequencies is ± 4 MHz. The relative intensity of the experimental ENDOR lines depend further critically on the spin relaxation properties, related to the temperature and microwave and rf power used—an effect which cannot be included in the calculations. Within all these limits we see a reasonable agreement between the experimental and predicted spectrum.

VII. CONCLUSION

Very high frequency EPR measurements (up to 324 GHz) and Q -band ENDOR measurements have been applied to the

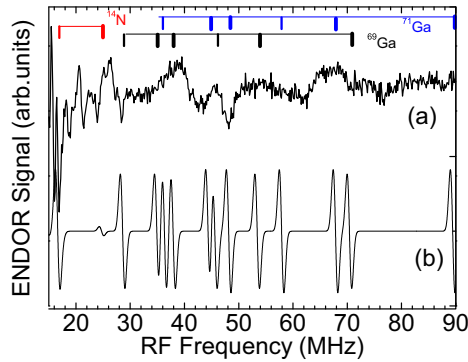


FIG. 8. (Color online) (a) Experimental ENDOR spectra measured at 6 K, at the central part of the EPR spectrum, for magnetic field parallel to the c axis; this spectrum is an averaged slice of the 2D spectrum shown in Fig. 7(a). (b) Calculated ENDOR spectrum assuming a constant linewidth of 1 MHz.

main paramagnetic defect introduced by room-temperature particle irradiation in n -type GaN. Our results confirm the attribution of this defect to the nitrogen split interstitial in the neutral charge state. This defect introduces a $(0/-)$ charge transition level 1.0 eV below the conduction-band minimum and pins the Fermi level for high fluences. As we observe the N interstitial, its counterpart, the nitrogen vacancy, should also have been generated by the irradiation. Whereas we have an indication from positron annihilation spectroscopy (PAS) [28] that the N vacancy is generated and stable, it is in the wrong diamagnetic charge state to be observable by EPR in heavily irradiated samples. The same argument is valid for the nonobservation of the Ga monovacancy [4,6]. Our PAS measurements [28] have shown it to be a dominant defect also in our samples, but due to the Fermi-level pinning by the N split interstitial at $E_{CB} - 1.0$ eV this defect is always in the diamagnetic $3-$ charge state and thus not observable by EPR. As n -type GaN has already annealing stages below $T = 300$ K for the Ga sublattice [18], the formation of complex defects due to the high mobility of Ga atoms and dynamic annealing during the room-temperature irradiation has also to be considered. Whereas nitrogen sublattice related defects have not been reported in other magnetic resonance studies, it is however probable that the neutral $(N-N)_N$ split interstitial has been observed before, but not recognized as such. Indeed, a so-called “deep donor” defect has been reported in ODMR studies of particle irradiated GaN [39] which shows compatible g values and overall linewidth

TABLE VI. N and Ga ENDOR frequencies in MHz for $B||c$ and $B \perp c$ given for low (LF) and high frequency (HF) conditions. Estimates of unresolved transitions below 16 MHz are also given (in brackets).

Isotope			N1	N2		
^{14}N	low frequency	$B c$	(3.7)	17.2		
^{14}N	high frequency	$B c$	(11.3)	24.8		
Isotope			Ga ₁	Ga ₂	Ga ₃	Ga ₄
^{69}Ga	low frequency	$B c$	45.7	28.7	(10.2)	(12.9)
^{71}Ga	low frequency	$B c$	57.9	36.2	(12.8)	(16.3)
^{69}Ga	high frequency	$B c$	70.7	53.7	35.2	37.9
^{71}Ga	high frequency	$B c$	89.8	68.2	44.8	48.3
^{69}Ga	low frequency	$B \perp c$	28.7	39.5	(12.1)	(11.6)
^{71}Ga	low frequency	$B \perp c$	36.2	50.0	(15.2)	(14.6)
^{69}Ga	high frequency	$B \perp c$	53.7	64.5	37.1	36.6
^{71}Ga	high frequency	$B \perp c$	68.3	82.0	47.2	46.6

of 170 G. As in these measurement the hf splitting was not resolved, no microscopic model could be proposed. In addition, the observation of a $S = 1/2$ center (labeled D2) was recently reported by EPR in n -type electron irradiated GaN [8], whereby the EPR pattern was resolved at 77 K exclusively. It shows a similar complex hf structure as well as comparable g values as the $(N-N)_N$ split interstitial center in the high-temperature state above 40 K. In Ref. [8], however, the spectrum was speculatively attributed to the gallium monovacancy associated with an oxygen first neighbor atom. However, this assignment is not supported by our modeling [28]. Finally, the importance of the nitrogen split interstitial defects in particle irradiated GaN shows many similarities to the case of diamond [44] and silicon carbide in which the stable configuration of the carbon interstitials is equally the split interstitial configuration.

ACKNOWLEDGMENTS

The numerical calculations were done using grants of computer time from the Paderborn Center for Parallel Computing (PC²) and the Höchstleistungs-Rechenzentrum Stuttgart (HLRS). The Deutsche Forschungsgemeinschaft (DFG), the Deutsche Akademische Austauschdienst (DAAD) und the Research Foundation-Flanders (FWO) are acknowledged for financial support. We thank A. Barra from the Laboratoire National des Champs Magnétiques Intenses for her help with the high frequency EPR measurements.

- [1] M. Linde, S. J. Uffring, G. D. Watkins, V. Härle, and F. Scholz, *Phys. Rev. B* **55**, R10177 (1997).
 [2] C. Bozdog, H. Przybylinska, G. D. Watkins, V. Harle, F. Scholz, M. Mayer, M. Kamp, R. J. Molnar, A. E. Wickenden, D. D. Koleske, and R. L. Henry, *Phys. Rev. B* **59**, 12479 (1999).
 [3] K. H. Chow, G. D. Watkins, A. Usui, and M. Mizuta, *Phys. Rev. Lett.* **85**, 2761 (2000).

- [4] G. D. Watkins, L. S. Vlasenko, and C. Bozdog, *Physica B* **308-310**, 62 (2001).
 [5] G. D. Watkins, K. H. Chow, P. Johannesen, L. S. Vlasenko, C. Bozdog, A. J. Zakrzewski, M. Mizuta, H. Sunakawa, N. Kuroda, and A. Usui, *Physica B* **340-342**, 25 (2003).
 [6] K. H. Chow, L. S. Vlasenko, P. Johannesen, C. Bozdog, G. D. Watkins, A. Usui, H. Sunakawa, C. Sasaoka, and M. Mizuta, *Phys. Rev. B* **69**, 045207 (2004).

- [7] P. Johannesen, A. Zakrzewski, L. S. Vlasenko, G. D. Watkins, A. Usui, H. Sunakawa, and M. Mizuta, *Phys. Rev. B* **69**, 045208 (2004).
- [8] N. T. Son, C. G. Hemmingsson, T. Paskova, K. R. Evans, A. Usui, N. Morishita, T. Ohshima, J. Isoya, B. Monemar, and E. Janzén, *Phys. Rev. B* **80**, 153202 (2009).
- [9] K. Saarinen, T. Suski, I. Grzegory, and D. C. Look, *Physica B* **308–310**, 77 (2001).
- [10] K. Saarinen, T. Suski, I. Grzegory, and D. C. Look, *Phys. Rev. B* **64**, 233201 (2001).
- [11] S. Hautakangas, V. Ranki, I. Makkonen, M. J. Puska, K. Saarinen, L. Liizkay, D. Seghier, H. P. Gislason, J. A. Freitas, R. L. Henry, X. Xu, and D. C. Look, *Physica B* **376–377**, 424 (2006).
- [12] S. Hautakangas, I. Makkonen, V. Ranki, M. J. Puska, K. Saarinen, X. Xu, and D. C. Look, *Phys. Rev. B* **73**, 193301 (2006).
- [13] F. Tuomisto, V. Ranki, D. C. Look, and G. C. Farlow, *Phys. Rev. B* **76**, 165207 (2007).
- [14] F. Tuomisto, *Appl. Surf. Sci.* **255**, 54 (2007).
- [15] F. Tuomisto, K. Saarinen, T. Paskova, B. Monemar, M. Bockowski, and T. Suski, *J. Appl. Phys.* **99**, 066105 (2006).
- [16] D. C. Look, D. C. Reynolds, J. W. Hemsley, J. R. Sizerlove, R. L. Jones, and R. J. Molnar, *Phys. Rev. Lett.* **79**, 2273 (1997).
- [17] D. C. Look, G. C. Farlow, P. J. Drevinski, and D. F. Bliss, *App. Phys. Lett.* **83**, 3525 (2003).
- [18] Z. Fang, G. Farlow, B. Claffin, and D. Look, *Proceedings of the 13th International Conference on Semiconducting and Insulating Materials, SIMC-XIII-2004* (IEEE, Beijing, 2004), p. 29.
- [19] D. C. Look, Z. Q. Fang, and B. Claffin, *J. Cryst. Growth* **281**, 143 (2005).
- [20] C. G. van de Walle and J. Neugebauer, *J. Appl. Phys.* **95**, 3851 (2004).
- [21] F. Gao, E. J. Bylaska, and W. J. Weber, *Phys. Rev. B* **70**, 245208 (2004).
- [22] H. Y. Xiao, F. Gao, X. T. Zu, and W. J. Weber, *J. Appl. Phys.* **103**, 123529 (2008).
- [23] H. Y. Xiao, F. Gao, X. T. Zu, and J. Weber, *J. Appl. Phys.* **105**, 123527 (2009).
- [24] U. Gerstmann, M. Rohrmüller, F. Mauri, and W. G. Schmidt, *Phys. Status Solidi C* **7**, 157 (2010).
- [25] H. Itoh, A. Kawasuso, T. Oshima, I. Nashiyama, S. Tanigawa, S. Misawa, H. Okumura, and S. Yoshida, *Phys. Status Solidi A* **162**, 173 (1997).
- [26] B. Aradi, A. Gali, P. Deak, J. E. Lowther, N. T. Son, E. Janzen, and W. J. Choyke, *Phys. Rev. B* **63**, 245202 (2001).
- [27] V. Y. Bratus, I. N. Makeeva, S. M. Okulov, T. L. Petrenko, T. T. Petrenko, and H. J. von Bardeleben, *Physica B* **308–310**, 621 (2001).
- [28] H. J. von Bardeleben, J. L. Cantin, U. Gerstmann, A. Scholle, S. Greulich-Weber, E. Rauls, M. Landmann, W. G. Schmidt, A. Gentils, J. Botsoa, and M. F. Barthe, *Phys. Rev. Lett.* **109**, 206402 (2012).
- [29] H. Vrielinck, H. DeCooman, Y. Karakirova, N. D. Yordanov, and F. Callens, *Radiat. Res.* **172**, 226 (2009); F. Loncke, H. De Cooman, N. M. Khaidukov, H. Vrielinck, E. Goovaerts, and F. Callens, *Phys. Chem. Chem. Phys.* **9**, 5320 (2007).
- [30] W. E. Carlos, J. A. Freitas, Jr., M. A. Khan, D. T. Olson, and J. N. Kuznia, *Phys. Rev. B* **48**, 17878 (1993).
- [31] A. Scholle, S. Greulich-Weber, D. J. As, Ch. Mietze, N. T. Son, C. Hemmingsson, B. Monemar, E. Janzén, U. Gerstmann, S. Sanna, E. Rauls, and W. G. Schmidt, *Physica Status Solidi B* **247**, 1728 (2010).
- [32] P. Stoll, EasySpin Program; <http://www.easyspin.org>.
- [33] J. P. Perdew, K. Burke, and M. Ernzerhof, *Phys. Rev. Lett.* **78**, 1396 (1997).
- [34] Ch.J. Pickard and F. Mauri, *Phys. Rev. Lett.* **88**, 086403 (2002).
- [35] P. Giannozzi *et al.*, *J. Phys.: Condens. Matter* **21**, 395502 (2009).
- [36] P. E. Blöchl, *Phys. Rev. B* **62**, 6158 (2000).
- [37] J. Heyd and G. E. Scuseria, *J. Chem. Phys.* **121**, 1187 (2004).
- [38] F. K. Koschnick, K. Michael, J. M. Spaeth, B. Beaumont, and P. Gibart, *Phys. Rev. B* **54**, R11042 (1996).
- [39] E. R. Glaser, T. A. Kennedy, W. E. Carlos, J. A. Freitas, Jr., A. E. Wickenden, and D. D. Koleske, *Phys. Rev. B* **57**, 8957 (1998).
- [40] M. Corti, A. Gabetta, M. Fanciulli, A. Svane, and N. E. Christensen, *Phys. Rev. B* **67**, 064416 (2003).
- [41] J. P. Yesinowski, *Phys. Status Solidi C* **2**, 2399 (2005).
- [42] I.-W. Park, H. Choi, H. J. Kim, H. W. Shin, S. S. Park, and S. H. Choh, *Phys. Rev. B* **65**, 195210 (2002).
- [43] G. Denninger, R. Beerhalter, D. Reiser, K. Maier, J. Schneider, T. Detchprom, and K. Hiramatsu, *Solid State Commun.* **99**, 347 (1996).
- [44] D. C. Hunt, D. J. Twitchen, M. E. Newton, J. M. Baker, T. R. Anthony, W. F. Banholzer, and S. S. Vagarali, *Phys. Rev. B* **61**, 3863 (2000).